Optics & Laser Technology 179 (2024) 111274

Contents lists available at ScienceDirect

Optics and Laser Technology

journal homepage: www.elsevier.com/locate/optlastec

Full length article

InP-based integrated optical frequency shifter for heterodyne detection applications

Pablo López-Querol [a,*], Alicia Soria-Gómez [a], Ana Quirce [b], José Manuel G. Tijero [a], Ignacio Esquivias [a], Antonio Pérez-Serrano [a]

[a] CEMDATIC-ETSI Telecomunicación, Universidad Politécnica de Madrid, 28040, Madrid, Spain
[b] Instituto de Física de Cantabria (IFCA), Universidad de Cantabria-CSIC, 39005, Santander, Spain

ARTICLE INFO

Keywords:
IQ modulator
Frequency shifter
Photonic integrated circuits
Heterodyne detection
Generic integration platform
InP

ABSTRACT

We present the design and characterization of an integrated optical frequency shifter based on an IQ modulator featuring standard building blocks from a generic photonic integration Indium Phosphide (InP) foundry. The device is conceived to be used in applications with low bandwidth requirements such as dual-comb spectroscopy or integrated low-cost LiDARs. An initial analytical study of the system was carried out and subsequently validated by simulations. Then, we obtained experimentally the most relevant parameters of the system and evaluated its performance under frequency shifter operation. Good performance up to 250 MHz is achieved, thus proving its suitability for the intended applications.

1. Introduction

Optical frequency shifters are used in many application fields including microwave photonics [1], optical communications [2], and frequency comb generation [3]. In particular, systems based on heterodyne detection, such as coherent LiDAR [4] or dual-comb spectrometers [5], have been realized using bulky acousto-optic modulators (AOMs). They are applied to shift the measured signal tens to hundreds of MHz away from the DC component thus minimizing the effects of 1/f noise and ensuring that the beat notes produced at both sides of the spectrum are unambiguously distinguished. For this, the suppression ratios (carrier suppression ratio, CSR, and sideband suppression ratio, SBSR) must be adequate to allow to resolve the shifted signal in the RF domain.

Recently, many efforts have been devoted to developing integrated AOMs [6,7]. Nevertheless, they have either been realized at expenses of hybrid integration, or they are not offered as building blocks (BBs) in generic integration platforms. Integrated frequency shifters based on single-sideband suppressed-carrier (SSB-SC) modulation using an IQ modulator [8,9] represent a suitable alternative to integrated AOMs. Frequency shifters based on IQ modulators have been demonstrated on silicon-based Photonic Integrated Circuits (PICs) achieving shifts up to 10 GHz, and a CSR, and SBSR between 16 and 23 dB [10]. In indium phosphide (InP) platforms, IQ modulators have been proposed as fast digital transmitters in coherent communication systems achieving rates up to 128 Gb/s [11]. However, as far as we know, their analog modulation and its application as optical frequency shifter have not been reported.

In this work, we demonstrate an integrated frequency shifter based on an IQ modulator fabricated through an open-access InP generic integration platform using standard BBs, thus allowing the development of an integrated system that could contain active devices such as lasers, as well as the compensation of the IQ modulator losses by means of Semiconductor Optical Amplifiers (SOAs). Nevertheless, the technology employed imposes some constraints and does not allow the implementation of single-drive push–pull operation mode of Mach–Zehnder modulators (MZMs). In addition, InP-based electro-optic phase modulators (EOPMs) require working in reverse bias to exploit electro-optic effect [12]. Furthermore, the fabrication tolerances introduce certain non-ideal characteristics in the components. To overcome the latter limitation, internal photodetectors (PDs) are included at the output of each MZM, allowing to extract the parameters of the system and for control purposes. All these peculiarities have motivated a detailed theoretical analysis of the proposed integrated frequency shifter. This comprehensive analysis encompasses all the mentioned characteristics and relies on measurable quantities, either on the internal PDs or at the output of the PIC. Good agreement is found between the analytical model, numerical simulations and experimental results. We report good performance up to 250 MHz with SBSRs greater than 15 dB.

The paper is organized as follows. Section 2 presents the different considerations followed during the design process and the theoretical

---

* Corresponding author.
E-mail address: pablo.lquerol@upm.es (P. López-Querol).

https://doi.org/10.1016/j.optlastec.2024.111274
Received 20 November 2023; Received in revised form 10 April 2024; Accepted 4 June 2024

model of our InP-based frequency shifter including all the characteristics commented above. The detailed development of this theoretical model is described in Appendix. The final PIC layout and fabrication aspects are discussed in Section 3. Experimental characterization and frequency shifting demonstration using the fabricated PIC are shown in Section 4. Finally, conclusions are summarized in Section 5.

2. Design and analysis

A conventional I–Q modulator consists of two identical MZMs arranged in parallel in the two branches (I and Q) of an interferometer. An additional phase shifter placed in one of the branches introduces a $\pi/2$ phase difference between the two arms. Since the work of Izutsu et al. [8], the fundamentals of the operation of these devices have been described by several authors [13,14].

To achieve the frequency shift, the MZMs are driven in push–pull mode ($V_A(t) = -V_B(t)$) so that each of their EOPMs induces opposite phase shifts ($\varphi_A(t) = -\varphi_B(t)$). At a minimum-transmission bias voltage, when each of the two MZMs is driven by cosine and sine RF signals, respectively, the output complex optical field, $E_{out}(t)$, is ideally an attenuated version of the input optical field, $E_{in}(t) = E_0 e^{j\omega_c t}$, frequency shifted by the modulation frequency, ω_s. If the modulation amplitude A relative to the half-wave voltage V_π, $R = A/V_\pi$, is small enough that the Jacobi–Anger expansion can be replaced by its first-order term, the output optical field is given by

$$E_{out} = \frac{1}{\sqrt{2}}\left(E^{I}_{out} + E^{Q}_{out}\right) = E_0 J_1(\pi R) e^{j(\omega_c \pm \omega_s)t} \tag{1}$$

where E^{I}_{out} and E^{Q}_{out} are the optical field outputs of the I- and Q-branch MZMs, respectively, and $J_1(\pi R)$ is the value at πR of the first order Bessel function of the first kind. The sign of the frequency shift in Eq. (1) depends on the relative sign of the modulating RF signals.

This general principle of operation has been implemented in the design of our integrated InP I–Q modulator. However, there are two important issues that need to be addressed by the proposed solution. Firstly, the operational differences between InP-based EOPMs and conventional $LiNbO_3$ modulators, specifically the requirement of reverse bias operation of the InP-based modulators. Secondly, the fabrication tolerances that may introduce uncontrolled non-idealities in the devices, leading to variations in performance.

The available EOPMs in InP platforms are based on InP/InGaAsP PIN junctions operating in reverse regime [15]. When these devices are reverse biased, the contribution of field (Kerr and mainly Pockels) and carrier effects (plasma and band-filling) lead to an effective phase shifting of the optical signal which is approximately linear with the bias voltage [16]. It is at this regime where the phase shift becomes more efficient and the modulator characteristics, such as the electrical bandwidth or the linearity of the phase shift with the bias voltage, are the most convenient. Therefore, the phase shift induced by the InP-based EOPMs is always negative according to the standard sign criterion [17]. This fact leads to a modification of the driving signals of the MZMs with respect to the conventional case.

In addition, V_π is inversely proportional to the length of the EOPM. Therefore, a longer EOPM is desirable to reduce the switching voltage and enhance compatibility with conventional laboratory equipment. However, extending the EOPM length will also result in a larger footprint and increased insertion losses. Therefore, there is a trade-off between making V_π small and the PIC footprint.

On the other hand, fabrication tolerances introduce uncontrolled differences in the response of each EOPMs, resulting in different V_π values. They also introduce voltage-independent, uncontrolled phase shifts that affect each component of the I–Q modulator differently. Therefore, the operation of the I–Q modulator depends critically on several parameters that can only be determined experimentally through a calibration process that requires experimental access to the power at several points in the circuit.

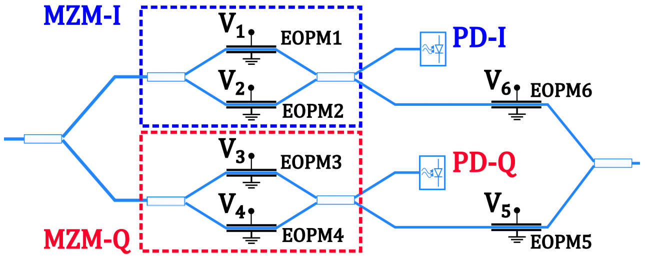

Fig. 1. Proposed IQ modulator scheme. MZM: Mach–Zehnder Modulator, PD: Photodiode.

To meet these requirements, the design shown schematically in Fig. 1 was implemented. It features two internal PDs that are implemented by using two 2×2 Multimode Interference (MMI) couplers. The PDs allow the measurement of the optical output power of each MZM, the analysis of which allows the determination of the key parameters of the device, as it will be explained later.

A detailed modeling of the operation of this design in terms of measurable parameters is provided in Appendix. In this section, we summarize the description of the operation and the basics of the calibration procedure.

The optical power measured by the photodiodes PD-I and PD-Q can be expressed as

$$P^{I}_{PD} = \frac{P_{in}}{2}\cos^2\left(\frac{\Delta\varphi_1 - \Delta\varphi_2 - \varphi^{I}_0 + \frac{\pi}{2}}{2}\right), \tag{2}$$

for the I branch and

$$P^{Q}_{PD} = \frac{P_{in}}{2}\cos^2\left(\frac{\Delta\varphi_3 - \Delta\varphi_4 - \varphi^{Q}_0 + \frac{\pi}{2}}{2}\right), \tag{3}$$

for the Q branch, where P_{in} is the input power, and $\Delta\varphi_i$ denotes the voltage-controlled phase shift of ith EOPM. φ^{I}_0 and φ^{Q}_0 are defined as $\varphi^{I}_0 = \varphi_{02} - \varphi_{01}$, and $\varphi^{Q}_0 = \varphi_{04} - \varphi_{03}$, where φ_{0i} represents the constant phase shift in the absence of applied voltage induced by each EOPM originated by the fabrication tolerances.

By measuring the powers in the PDs for suitable ranges of static driving voltages applied to each EOPM and using Eqs. (2) and (3), not only the values of V_π of each EOPM, but also φ^{I}_0 and φ^{Q}_0 can be determined experimentally, as it will be shown in Section 4.2. As it will become clear later, these are the key parameters for setting the operating conditions for the integrated I–Q modulator to work as a frequency shifter.

Due to the requirement of operation under reverse voltages, the condition of a cosine optical field at the output of each MZM cannot be fulfilled just by driving each EOPM with opposite voltages to get opposite phase shifts (push–pull mode). Instead, as shown in Appendix, the phase conditions are

$$\Delta\varphi_{1,3} - \varphi^{I,Q}_0 - \frac{\pi}{2} = 2\pi n - \Delta\varphi_{2,4}, \tag{4}$$

expressed in terms of $\varphi^{I,Q}_0$. This expression should be fulfilled for values of n that always guarantee reverse drive voltages. If minimum-transmission DC bias voltages

$$V_{2b,4b} = -\frac{V_{\pi 2,4}}{2} \tag{5}$$

are chosen for the EOPMs 2 and 4, respectively, and assuming $R \leq 0.5$, the fulfillment of Eq. (4) imposes the values for the minimum-transmission DC bias voltages for EOPMs 1 and 3, being

$$V_{1b,3b} = \begin{cases} -V_{\pi 1,3}\left(1 - \frac{\varphi^{I,Q}_0}{\pi}\right) & for\ -1 \leq \frac{\varphi^{I,Q}_0}{\pi} \leq 1 - R \\ -V_{\pi 1,3}\left(3 - \frac{\varphi^{I,Q}_0}{\pi}\right) & for\ 1 - R \leq \frac{\varphi^{I,Q}_0}{\pi} \leq 1 \end{cases} \tag{6}$$

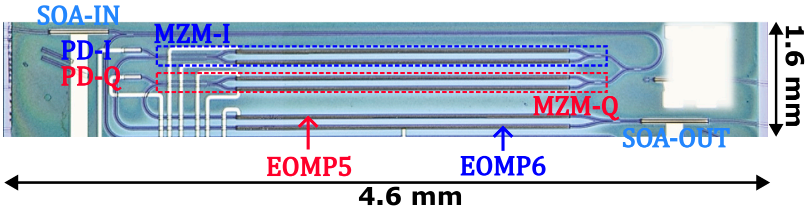

Fig. 2. Photograph of the fabricated PIC. SOA: Semiconductor Optical Amplifier, MZM: Mach–Zehnder Modulator, PD: Photodetector, EOPM: Electro-Optic Phase Modulator.

where the values of n have been chosen to minimize in each case the required reverse voltage, $n = -1$ and $n = -2$, respectively. The key role played by V_π of each EOPM and the phase parameters φ_0^I and φ_0^Q in the operation conditions of the frequency shifter is apparent.

In summary, for operation of the I–Q modulator as a frequency shifter the driving voltages of the EOPM$_i$ (i =1,2,3,4) should be

$$V_1 = V_{1b} - RV_{\pi 1}\sin(\omega_s t) \tag{7a}$$

$$V_2 = V_{2b} - RV_{\pi 2}\sin(\omega_s t) \tag{7b}$$

$$V_3 = V_{3b} \mp RV_{\pi 3}\cos(\omega_s t) \tag{7c}$$

$$V_4 = V_{4b} \mp RV_{\pi 4}\cos(\omega_s t) \tag{7d}$$

where the bias voltages are given by Eqs. (5) and (6).

Finally, EOPM5 and EOPM6 are used to ensure the necessary quadrature between the signals coming from the two branches. This can be achieved by simply setting the voltage V_5 applied to the EOPM5 to zero, and driving the EOPM6 with the DC voltage

$$V_6 = \begin{cases} V_{\pi 6}\left(\frac{1}{2} - \frac{\beta}{\pi}\right) & for\ \frac{1}{2} \le \frac{\beta}{\pi} \le 1 \\ V_{\pi 6}\left(-\frac{3}{2} - \frac{\beta}{\pi}\right) & for\ -1 \le \frac{\beta}{\pi} \le \frac{1}{2} \end{cases} \tag{8}$$

for $n = 0$ and $n = -1$, respectively. The voltage $V_{\pi 6}$ is the half-wave voltage of EOPM6 and β is a phase term defined in Appendix. Both parameters can be determined experimentally by analyzing the dependence on V_6 of the power measured at the output of the device. This power is given by

$$P_{out} = P_{in}\cos^2\left[\frac{1}{2}\left(\frac{V_6}{V_{\pi 6}}\pi + \beta\right)\right]. \tag{9}$$

under the appropriated DC bias voltages V_1, V_2, V_3 and V_4 detailed in Appendix.

In summary, an analytical model has been proposed for the intended operation of the device as a frequency shifter. The driving signals of each EOPM have been determined, taking into account the effects and terms arising from non-idealities caused by fabrication tolerances. The experimental determination of these non-ideal aspects is made possible by the presence of internal PDs. By driving the EOPMs with the signals specified in Eqs. (5)–(8), the proposed system effectively induces a frequency shift of the input optical signal.

3. PIC layout, simulation and fabrication

The initial design and simulations of the system were performed using VPIphotonics VPIcomponentMaker Photonic Circuits [18], while the final design and layout was generated using Nazca Design [19]. To do so, specific libraries from the Process Design Kit (PDK) of the foundry were used. The PIC has been fabricated by SMART Photonics [20] in a multi-project wafer (MPW) run through the open access platform JePPIX (Joint European Platform for Photonic Integration of Components and Circuits) [21].

This platform features active and passive standarized BBs based on InP. The waveguides used in this PIC feature a 2 μm width and are based on a deeply etched structure consisting on a p-InP, n-Q1.25 and n-InP layer stack. The losses of these waveguides are 3 dB/cm. The active BBs include an intrinsic layer consisting in a Multi-Quantum Well (MQW) structure. Further details on the fabrication processes and the platform can be found in [22,23].

Fig. 2 shows a photograph of the fabricated device (b). The chip has an optical input and an optical output. Both input and output waveguides are 7° tilted and the facets are antireflection coated. Light from an external source is injected into the chip through the input waveguide and boosted by a 350 μm-long SOA, SOA-IN. The input optical signal is divided by a 1 × 2 MMI coupler into the I and Q branches, respectively. Each branch has a dual-drive MZM, which consist in two parallel 2-mm-long EOPMs (In MZM-I, EOPM1 and EOPM2 and in MZM-Q, EOPM3 and EOPM4, respectively). The length of the EOPMs has been chosen to achieve a V_π value around 4.5 V according to simulations. The optical signals coming from each EOPM are combined and then divided using a 2 × 2 MMI coupler. The latter has been introduced to measure the output of each MZM with an internal PD (PD-I and PD-Q). After each MZM, a 2-mm-long EOPM is used to shift the phase of the optical signal and force I and Q to be in quadrature (EOPM5 and EOPM6). Furthermore, it is important to mention that the optical paths of the I and Q branches are not identical, a decision made to achieve a more compact design. Although this results in additional I-branch losses (approximately 0.1 dB), it is estimated that they should not have a significant impact on device performance. Finally, the outputs of these EOPMs are combined by a 2 × 1 MMI coupler and amplified by a 400 μm-long SOA (SOA-OUT).

Regarding the electrical connections, the PIC has ten DC electrical pads for biasing the different blocks and measuring the internal PDs and a common n-type substrate. The EOPMs use lumped electrodes as electrical contacts instead of traveling-wave electrodes. This limits the maximum modulation bandwidth to hundreds of MHz but simplifies the electrical design of the EOPMs and impedance matching issues. Nevertheless, these frequency ranges are suitable for the intended applications.

Simulations of the PIC layout have been conducted to check the proposed design and theoretical model using the PDK provided by the foundry. Fig. 3 shows the simulated optical spectra at various points of the system when the signals driving the EOPMs correspond to Eqs. (5)–(8) for a frequency shift of 100 MHz, with $R = 0.4$. Fig. 3(a) illustrates the simulated optical spectrum incident on the internal PD-I, while Fig. 3(b) presents the simulated optical spectrum at the output of the MZM-I. Since the MZM is biased at a minimum transmission point, the carrier and odd harmonics are sent to the PD branch while the even harmonics are sent to the output branch. These results are identical for the Q branch. In Fig. 3(b), it can be noticed that the carrier is effectively suppressed (approximately 38 dB) and only the first-order sidebands are significant.

Fig. 3(c) and (d) show the simulated optical spectra at the output of the system for positive and negative frequency shifts, respectively. In both cases, the optical carrier remains suppressed. By ensuring that the I and Q branches are in quadrature, the output signals from the MZMs interfere destructively for one of the sidebands, leading to its effective suppression and achieving SSB-SC modulation. Similar results are obtained for different frequency shifts, which validates qualitatively the theoretical model.

Fig. 6 shows a sweep of the bias voltage of EOPM6 while the EOPM5 has been set to $V_5 = 0$ V for simplicity. In this manner, β is determined

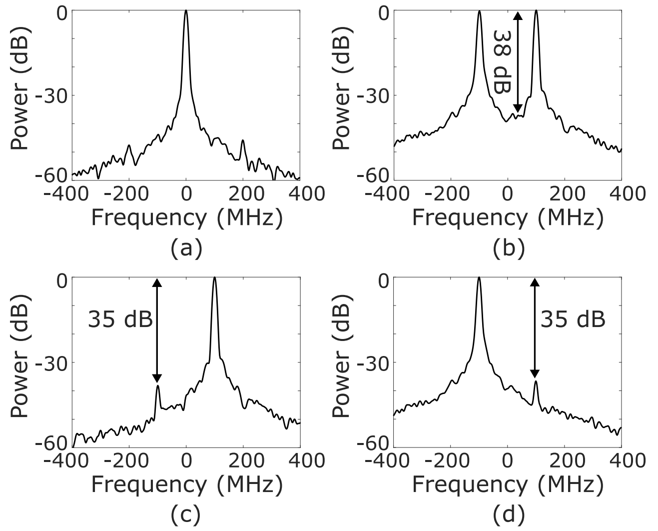

(a) (b) (c) (d)

Fig. 3. Simulated spectra of the optical field in frequency shifter operation for f_s = ±100 MHz at (a) the PD-I input; (b) the MZM-I output; and the output of the system for a (c) positive (d) and negative shift. The resolution of the OSA has been set to 10 MHz to adequate the results to the measuring system used in the experiments. All the spectra are normalized.

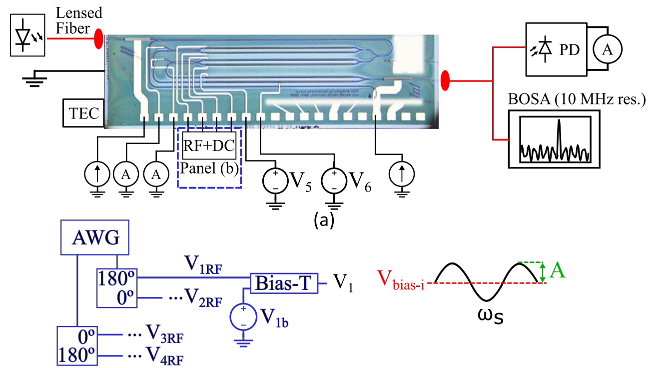

(a)

(b)

Fig. 4. (a) Experimental setup for the characterization of the PIC and (b) driving scheme for the EOPMs. The RF signal is combined with a DC bias through a Bias-Tee. In this way, the modulating signal consist in a DC component (V_{ib}) plus a RF signal with frequency ω_s and amplitude A_i. TEC: Thermoelectric Cooler, AWG: Arbitrary Waveform Generator, PD: Photodiode, BOSA: Brillouin Optical Spectrum Analyzer.

taking into account Eq. (A.21). The V_π of the modulator is obtained, as in the previous case, from the voltage difference between a maximum and a minimum.

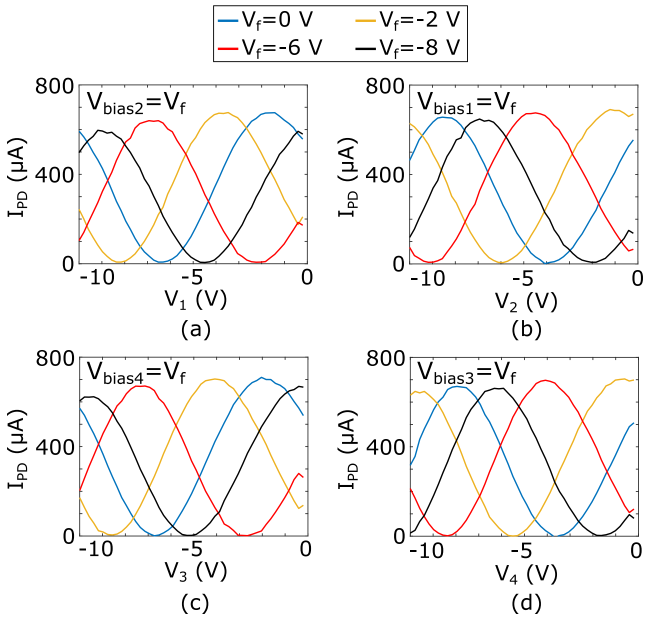

(a) (b) (c) (d)

Fig. 5. Response of the MZMs measured at the internal photodiodes for different DC bias voltages. (a) Bias voltage sweep of EOPM1 for different biases of EOPM2, (b) bias voltage sweep of EOPM2 for different biases of EOPM1, (c) bias voltage sweep of EOPM3 for different biases of EOPM4 and (d) bias voltage sweep of EOPM4 for different biases of EOPM3.

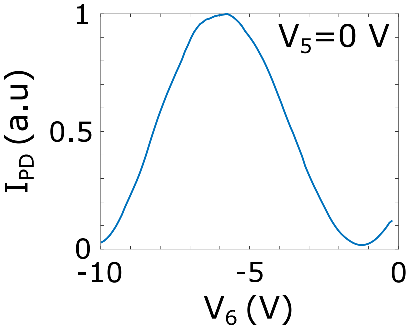

Fig. 6. Measured signal at the output of the device when V_5 = 0 V and V_6 is swept. We can extract β using Eq. (A.21).

4. Experimental results

4.1. Experimental setup

The fabricated PIC is experimentally characterized using the setup shown in Fig. 4(a). Each individual MZM modulator is characterized using the internal PDs, and the whole system performance is analyzed through the optical output, which is gathered by a lensed fiber placed at the output of the PIC. The output is measured simultaneously in a Brillouin Optical Spectrum Analyzer (BOSA) with a resolution of 10 MHz and in an external PD. The input light is injected by a narrow-linewidth (10 kHz, nominal) external laser (PurePhotonics PPL300) centered at a wavelength of 1550 nm, also using a lensed fiber. This input fiber is aligned by measuring and maximizing the injected power at the internal PDs.

Several current and voltage sources are used to power up the chip. The input and output SOAs are biased with a current of 80 mA to boost the power at the input and at the output, respectively. The photocurrents generated by the internal and external PDs are measured with several multimeters. The driving scheme used for the EOPMs of the MZMs is detailed in Fig. 4(b). Two outputs from an Arbitrary Waveform Generator (Tektronix AWG70002B) deliver the needed RF signals at 0° and 90° of phase each, which are later combined with a DC component using a Bias-Tee.

The chip is mounted on a copper mount for thermal control, which is done through a thermoelectric cooler (TEC) and a temperature controller operating at 25 °C. The electrical access to the PIC is made through 20 DC electrical probes.

4.2. Characterization of the PIC and parameter extraction

Firstly, the individual MZMs in the system are characterized to obtain the important parameters that have been described in Section 3 and will allow to drive the system as a Frequency Shifter/SSB-SC

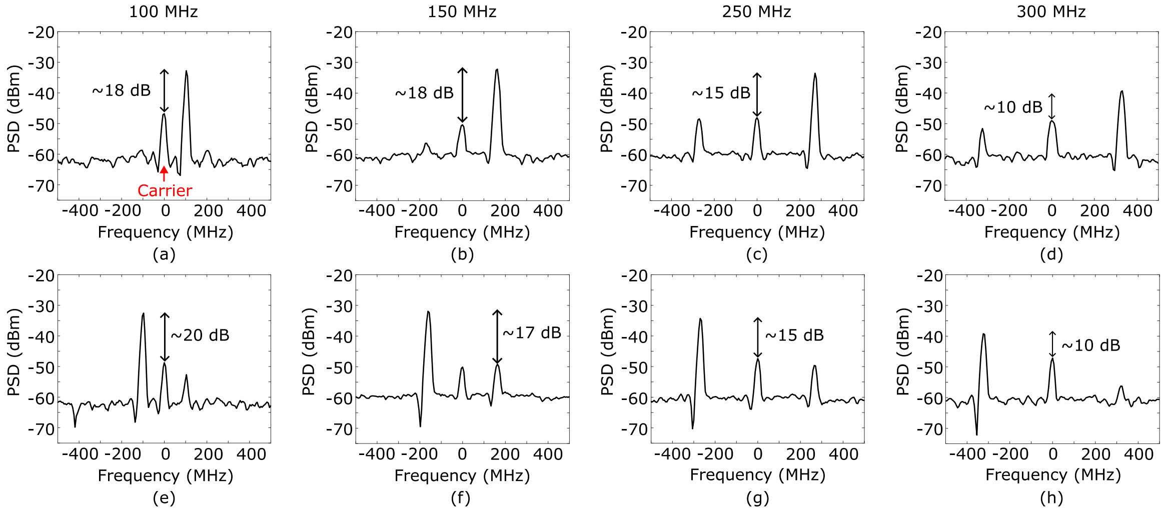

Fig. 7. Measured frequency shifts at different frequencies. Each column shows equal opposite shifts. The reference frequency corresponds to a wavelength of 1550 nm.

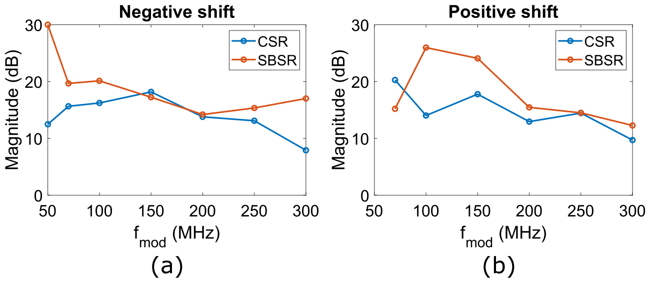

Fig. 8. CSR and SBSR evolution with modulation frequency for negative (a) and positive (b) frequency shifts. The modulation frequency ranges from 50 MHz to 300 MHz.

modulator. Fig. 5 shows the characterization of each MZM. To perform this response, the driving voltage of one of the EOPMs is swept while the other is biased with a fixed voltage (V_f). In this way, the response of each MZM is obtained as a function of the bias voltages of each EOPM. The V_π is measured as the voltage difference between constructive interference (maximum) and destructive interference (minimum).

From the analytical model described in Appendix, we can identify this response with the expressions given in Eqs. (2) and (3). In this way, the unknown values of φ_0^I and φ_0^Q can be determined. In contrast with other MZM based on $LiNbO_3$, the response has been observed to be very stable over time, which facilitates the measurement of system parameters. However, a certain decrease on the maximum photocurrent value can be observed in Fig. 5 when increasing the reverse voltage of the EOPMs. This is associated with the propagation losses increasing with the electrical field strength. These propagation losses increase due to the electro-absorption, caused by the Franz–Keldysh effect [24].

The characterization of the device provided the most relevant parameters of the system, which are indicated in Table 1.

4.3. Frequency shifter demonstration and performance

Based on the measured system parameters of Table 1, the driving signals of each EOPM to operate the IQ modulator as a frequency shifter are defined following Eqs. (7a)–(7d) and Eq. (8). The bias voltages values are $V_{1b} = -2.95$ V, $V_{2b} = -2.23$ V, $V_{3b} = -3.72$ V, $V_{4b} = -2.41$ V, $V_5 = 0$ V and $V_6 = -1.7$ V. Amplitude modulations A_i resulting in a low modulation depth, $R = 0.05$, were initially considered. This ensures that the modulator operates in the small signal regime. However, fine-tuning of bias voltages and modulation amplitudes around these values was necessary to optimize performance. The system performance is measured through the carrier suppression ratio (CSR) and the sideband suppression ratio (SBSR), defined as the power relation between the peaks of the shifted component and the peaks of the carrier and the sideband, respectively. Fig. 7 shows the measured spectra at the output of the PIC using the BOSA for different frequency shifts. The measurement resolution is limited by the BOSA to 10 MHz. Each column corresponds to the same shift and opposite signs. The sign of the shift can be easily controlled either with the phase of the harmonic RF signals which drive EOMP3 and EOPM4 either with the bias voltage of the EOPM6. Our frequency shifter features a CSR always above 15 dB for frequencies lower than 250 MHz and deteriorates with increasing frequency shifts, being reduced to 10 dB at 300 MHz. A SBSR above 15 dB is also maintained. These results have been observed to be very stable over time.

Table 1
Parameter values of the system experimentally determined.

Parameter	Value	Units
$V_{\pi 1}$	4.54	V
$V_{\pi 2}$	4.46	V
$V_{\pi 3}$	4.51	V
$V_{\pi 4}$	4.82	V
$V_{\pi 6}$	4.28	V
φ_0^I	1.1	rad
φ_0^Q	0.55	rad
β	0.29	rad

Fig. 8 shows the evolution of the device performance in terms of CSR and SBSR with the modulation frequency for negative (a) and positive (b) frequency shifts, ranging from 50 MHz up to 300 MHz. This frequency range is particularly relevant for the intended applications, as it enables heterodyne detection with a low bandwidth. As it can be observed, the performance deteriorates by increasing the frequency, and above 300 MHz (not shown) the device is not useful as frequency shifter.

From the point of view of the targeted applications, when performing heterodyne detection the signal of interest (either the positive or negative sideband, depending on the sign of the shift) is detected around the shift frequency, while the remaining carrier is detected around zero frequency and its presence does not affect signal detection, provided that the signal bandwidth does not reach the carrier region. Then carrier presence is not an important problem, although it implies a loss of power. However, with a CSR above 10 dB this loss is not significant.

On the other hand, the residual opposite sign frequency component appears as a mirrored version of the signal of interest in the same frequency range. If the SBSR is above 15 dB, the signal of interest can be effectively discriminated.

The degradation in the performance with increasing frequency is attributed to the low bandwidth of the lumped electrodes of the EOPMs and to the non-idealities of the system. In addition, the physical effects involved on the EOPM phase shifting mechanism also have a certain dependence on the incoming optical power and the light polarization, which has not been analyzed. Furthermore, a qualitative agreement has been observed between the simulations and the experimental measurements.

5. Conclusions

We have designed, analyzed and characterized an integrated frequency shifter/SSB-SC modulator on a PIC, conceived for low bandwidth heterodyne detection systems. The system is based on an IQ modulator which features standard BBs from the PDK of a generic integration InP foundry.

An initial analytical study of the system has been carried out, taking into account the features of the device and some of the customized aspects and fabrication tolerances of the components that could significantly affect the system performance, proposing an analytical model to understand its operation. This analytical model has been validated with good qualitative agreement through numerical simulation that have been carried out utilizing the PDK from the foundry and considering the physical layout of the device for a more realistic approach.

The most important parameters to be controlled regarding the operation of the system as a frequency shifter have been identified and defined. Those parameters have been determined experimentally with the help of the internal PDs. The inclusion of these devices and their measurements allow to characterize the fundamental operation of each MZM and define the modulating signals.

The operation of the PIC as frequency shifter has been demonstrated with good performance up to 250 MHz, meeting the requirements of the intended applications. The carrier suppression, measured through the CSR, and the sideband suppression, measured through the SBSR, are always greater than 15 dB below 250 MHz. Above 250 MHz a performance degradation is observed, worsening the CSR to 10 dB. We attribute this limitation to the non-idealities of the system and to the low bandwidth of the lumped electrodes of the EOPMs. Although the maximum shift is modest compared to some of the very high performance frequency shifters based on passive platforms [9,10], implementing such a system on an active platform has a great interest and potential to combine it with other functionalities that can only be achieved on active platforms. In addition, the achieved performance makes the system suitable for using the proposed PIC in low bandwidth heterodyne detectors for integrated low-cost coherent LiDARs and dual-comb spectrometers.

CRediT authorship contribution statement

Pablo López-Querol: Writing – original draft, Software, Methodology, Investigation, Formal analysis, Data curation, Conceptualization. **Alicia Soria-Gómez:** Investigation, Conceptualization. **Ana Quirce:** Writing – review & editing, Supervision, Project administration, Methodology, Investigation, Formal analysis. **José Manuel G. Tijero:** Writing – review & editing, Supervision, Methodology, Investigation, Funding acquisition, Formal analysis. **Ignacio Esquivias:** Writing – review & editing, Supervision, Project administration, Methodology, Investigation, Funding acquisition, Conceptualization. **Antonio Pérez-Serrano:** Writing – review & editing, Supervision, Methodology, Investigation, Funding acquisition, Formal analysis, Conceptualization.

Declaration of competing interest

The authors declare that they have no known competing financial interests or personal relationships that could have appeared to influence the work reported in this paper.

Data availability

Data will be made available on request.

Acknowledgments

This work was supported by the grants TED2021-131957B-100 and PID2021-1234590B-C21 funded by Ministerio de Ciencia e Innovación (Spain), MCIN/AEI/10.13039/501100011033 and by the European Union NextGenerationEU/PRTR and ERDF “A way of making Europe”.

A.Q. acknowledges the grant PID2021-123459OB-C22 funded by MCIN/AEI/10.13039/501100011033/FEDER, UE. and the financial support from Beatriz Galindo program, Ministerio de Ciencia, Innovación *y* Universidades (Spain).

Appendix. Detailed development of the analytical model

The expression of the optical field reaching the internal PDs and at the output of the MZMs are given by

$$E^{I}_{PD}(t) = \frac{E_{in}(t)}{2\sqrt{2}}\left(e^{j(\varphi_1(t)+\frac{\pi}{2})} + e^{j\varphi_2(t)}\right), \tag{A.1}$$

$$E^{I}_{out}(t) = \frac{E_{in}(t)}{2\sqrt{2}}\left(e^{j\varphi_1(t)} + e^{j(\varphi_2(t)+\frac{\pi}{2})}\right), \tag{A.2}$$

for the I branch, and

$$E^{Q}_{PD}(t) = \frac{E_{in}(t)}{2\sqrt{2}}\left(e^{j(\varphi_3(t)+\frac{\pi}{2})} + e^{j\varphi_4(t)}\right), \tag{A.3}$$

$$E^{Q}_{out}(t) = \frac{E_{in}(t)}{2\sqrt{2}}\left(e^{j\varphi_3(t)} + e^{j(\varphi_4(t)+\frac{\pi}{2})}\right), \tag{A.4}$$

for the Q branch. In these expressions $\varphi_i(t) = \varphi_{0i} + \Delta\varphi_i(t)$ is the total phase shift induced by each EOPM, including the voltage independent term φ_{0i} and the voltage dependent term $\Delta\varphi_i(t) = \pi V_i(t)/V_{\pi i}$. It is convenient to rewrite Eqs. (A.2) and (A.4) as

$$E^{I}_{out}(t) = \frac{E_{in}(t)}{2\sqrt{2}} e^{j\alpha_I}\left(e^{j\left[\Delta\varphi_1-\left(\varphi_0^I+\frac{\pi}{2}\right)\right]} + e^{j\Delta\varphi_2}\right), \tag{A.5}$$

$$E^{Q}_{out}(t) = \frac{E_{in}(t)}{2\sqrt{2}} e^{j\alpha_Q}\left(e^{j\left[\Delta\varphi_3-\left(\varphi_0^Q+\frac{\pi}{2}\right)\right]} + e^{j\Delta\varphi_4}\right), \tag{A.6}$$

respectively, where $\alpha_I = \varphi_{02} + \pi/2$, $\alpha_Q = \varphi_{04} + \pi/2$, $\varphi_0^I = \varphi_{02} - \varphi_{01}$ and $\varphi_0^Q = \varphi_{04} - \varphi_{03}$.

The photocurrent measured at the internal PDs is directly proportional to the optical power reaching the PDs. The optical power is related to the optical field as $P = |E|^2$. Consequently, it can be written as

$$P^{I}_{PD} = \frac{P_{in}}{2}\cos^2\left(\frac{\Delta\varphi_1 - \Delta\varphi_2 - \varphi_0^I + \frac{\pi}{2}}{2}\right), \tag{A.7}$$

for the PD at the I branch and

$$P^{Q}_{PD} = \frac{P_{in}}{2}\cos^2\left(\frac{\Delta\varphi_3 - \Delta\varphi_4 - \varphi_0^Q + \frac{\pi}{2}}{2}\right), \tag{A.8}$$

for the PD at the Q branch. These expressions correspond to Eqs. (2)–(3) of Section 3 and allow the experimental determination of $V_{\pi i}$ (i = 1,2,3,4) and φ_0^I and φ_0^Q as commented in the main text.

According to Eqs. (A.5) and (A.6), in order to get output signals in the I and Q branches $E_{out}^{I,Q}$, of the form

$$E_{out}^{I,Q} = \frac{E_{in}}{\sqrt{2}} e^{j\alpha_{I,Q}} \cos \Delta\varphi_{2,4}, \tag{A.9}$$

the general phase condition

$$\Delta\varphi_{1,3} - \varphi_0^{I,Q} - \frac{\pi}{2} = 2\pi n - \Delta\varphi_{2,4} \tag{A.10}$$

should be fulfilled for an integer n. This expression corresponds with Eq. (4) in the main text. In addition, the requirement of negative driving voltages at all times imposes a limitation for the values of n that determine the minimum reverse bias voltages of each modulator.

Choosing $V_{2b} = -V_{\pi 2}/2$ as the minimum-transmission bias voltage at the I branch, ensures that the modulation voltage $V_2(t) = V_{2b} + RV_{\pi 2}\sin\left(\omega_s t\right)$ is always negative for relatively high values of the modulation depth $R \leq 0.5$. The condition defined in Eq. (A.10) imposes $V_1(t) = V_{1b} - RV_{\pi 1}\sin\left(\omega_s t\right)$, with $V_{1b} = V_{\pi 1}\left(2n + 1 + \varphi_0^I/\pi\right)$ and therefore, the minimum reverse bias voltage $|V_{1b}|$ ensuring $V_1(t) < 0$ depends on the phase difference φ_0^I, resulting

$$V_{1b} = \begin{cases} -V_{\pi 1}\left(1 - \frac{\varphi_0^I}{\pi}\right) & for\ -1 \leq \frac{\varphi_0^I}{\pi} \leq 1 - R \\ -V_{\pi 1}\left(3 - \frac{\varphi_0^I}{\pi}\right) & for\ 1 - R \leq \frac{\varphi_0^I}{\pi} \leq 1 \end{cases} \tag{A.11}$$

for $n = -1$ and $n = -2$, respectively, where φ_0^I has been chosen to range between $-\pi$ and π.

For the Q branch, a similar reasoning for $V_4(t) = V_{4b} \pm RV_{\pi 4}\cos\left(\omega_s t\right)$, leads to $V_3(t) = V_{3b} \mp RV_{\pi 3}\cos\left(\omega_s t\right)$ with

$$V_{3b} = \begin{cases} -V_{\pi 3}\left(1 - \frac{\varphi_0^Q}{\pi}\right) & for\ -1 \leq \frac{\varphi_0^Q}{\pi} \leq 1 - R \\ -V_{\pi 3}\left(3 - \frac{\varphi_0^Q}{\pi}\right) & for\ 1 - R \leq \frac{\varphi_0^Q}{\pi} \leq 1 \end{cases} \tag{A.12}$$

for $n = -1$ and $n = -2$, respectively.

In summary, the RF driving voltages of each phase modulator should be

$$V_1 = V_{1b} - RV_{\pi 1}\sin(\omega_s t) \tag{A.13a}$$

$$V_2 = V_{2b} - RV_{\pi 2}\sin(\omega_s t) \tag{A.13b}$$

$$V_3 = V_{3b} \mp RV_{\pi 3}\cos(\omega_s t) \tag{A.13c}$$

$$V_4 = V_{4b} \mp RV_{\pi 4}\cos(\omega_s t) \tag{A.13d}$$

where the corresponding DC bias voltages are given by

$$V_{1b} = \begin{cases} -V_{\pi 1}\left(1 - \frac{\varphi_0^I}{\pi}\right) & for\ -1 \leq \frac{\varphi_0^I}{\pi} \leq 1 - R \\ -V_{\pi 1}\left(3 - \frac{\varphi_0^I}{\pi}\right) & for\ 1 - R \leq \frac{\varphi_0^I}{\pi} \leq 1 \end{cases} \tag{A.14a}$$

$$V_{2b} = -\frac{V_{\pi 2}}{2} \tag{A.14b}$$

$$V_{3b} = \begin{cases} -V_{\pi 3}\left(1 - \frac{\varphi_0^Q}{\pi}\right) & for\ -1 \leq \frac{\varphi_0^Q}{\pi} \leq 1 - R \\ -V_{\pi 3}\left(3 - \frac{\varphi_0^Q}{\pi}\right) & for\ 1 - R \leq \frac{\varphi_0^Q}{\pi} \leq 1 \end{cases} \tag{A.14c}$$

$$V_{4b} = -\frac{V_{\pi 4}}{2} \tag{A.14d}$$

These expressions correspond to Eqs. (5) and (6) in the main text.

Finally, the requirement of a $\pi/2$ phase difference between the signals coming from the two branches can be fulfilled by biasing one of the phase modulators 5 and 6 with an adequate voltage. Assuming that only EOPM 6 is biased, the phase shifts induced by each modulator are φ_{05} and $\varphi_{06} + \Delta\varphi_6(V_6)$, where φ_{05} and φ_{06} are the voltage independent phase shifts and $\Delta\varphi_6(V_6) = \pi V_6/V_{\pi 6}$ is the voltage dependent phase shift induced by EOPM 6. Therefore, the signal at the output of the entire device can be written as

$$E_{out}(t) = \frac{E_{in}(t)}{2}[e^{j(\alpha_I + \varphi_{06} + \Delta\varphi_6)}\cos\Delta\varphi_2 + \\ e^{j(\alpha_Q + \varphi_{05})}\cos\Delta\varphi_4]. \tag{A.15}$$

It is convenient to write this expressions in terms of the uncontrolled phases $\beta_I = \alpha_I + \varphi_{06}$ and $\beta_Q = \alpha_Q + \varphi_{05}$, and the voltage controlled $\Delta\varphi_6$, resulting in

$$E_{out}(t) = \frac{E_{in}(t)}{2}[e^{j(\beta_I + \Delta\varphi_6)}\cos\Delta\varphi_2 + e^{j\beta_Q}\cos\Delta\varphi_4],$$

that, in turn can be written in terms of $\beta = \beta_I - \beta_Q$ which can be experimentally determined. Then, the optical field at the output is

$$E_{out}(t) = \frac{E_{in}(t)}{2}e^{j\beta_Q}[e^{j(\beta + \Delta\varphi_6)}\cos\Delta\varphi_2 + \cos\Delta\varphi_4], \tag{A.16}$$

and the voltage V_6 should ensure the following phase condition

$$\frac{V_6\pi}{V_{\pi 6}} + \beta = \frac{\pi}{2} + 2\pi n \tag{A.17}$$

Therefore, the minimum negative bias voltage V_6 is given by

$$V_6 = \begin{cases} V_{\pi 6}\left(\frac{1}{2} - \frac{\beta}{\pi}\right) & for\ \frac{1}{2} \leq \frac{\beta}{\pi} \leq 1 \\ V_{\pi 6}\left(-\frac{3}{2} - \frac{\beta}{\pi}\right) & for\ -1 \leq \frac{\beta}{\pi} \leq \frac{1}{2} \end{cases} \tag{A.18}$$

for $n = 0$ and $n = -1$, respectively. This expression corresponds to Eq. (8) in the main text.

By substituting Eq. (A.17) into Eq. (A.16) and substituting also $\Delta\varphi_2(t)$ and $\Delta\varphi_4(t)$ to the corresponding RF driving voltages given by Eq. (A.13) the output optical field read as

$$E_{out}(t) = \frac{E_{in}(t)}{2}e^{j\beta_Q}[j\sin\left(R\pi\sin\omega_s t\right) \pm \\ \sin\left(R\pi\cos\omega_s t\right)], \tag{A.19}$$

If we assume that R is small enough, Eq. (A.19) can be approximated by the leading term of its Jacobi–Anger expansion, getting

$$E_{out}(t) = E_{in}(t)J_1(\pi R)\, e^{j\beta_Q}\left[j\sin\omega_s t \pm \cos\omega_s t\right]$$

that can be written in the form

$$E_{out}(t) = \pm E_0 J_1(\pi R)\, e^{j\beta_Q} e^{j(\omega_c \pm \omega_s)t} \tag{A.20}$$

where it is apparent that it is actually the frequency shifted response of the device to the input optical field in an amount of ω_s or $-\omega_s$ depending on the sign chosen in Eqs. (A.13c) and (A.13d).

Finally, as mentioned in the main text, both $V_{\pi 6}$ and β can be determined experimentally by analyzing the dependence on V_6 of the power measured at the output of the device when appropriate DC bias voltages V_1, V_2, V_3 and V_4 are selected. These voltages should verify that the phase shifts induced by them satisfy the phase conditions (Eq. (A.10)) and $\Delta\varphi_2 = \Delta\varphi_4 = \Delta\varphi$. Under these driving conditions, if $\Delta\varphi = -\pi$ (to maximize the power), Eq. (A.16) becomes

$$E_{out}(t) = -\frac{E_{in}(t)}{2}e^{j\beta_Q}[e^{j(\beta + \Delta\varphi_6)} + 1]$$

and the corresponding power is given by

$$P_{out} = P_{in}\cos^2\left[\frac{1}{2}\left(\frac{V_6}{V_{\pi 6}}\pi + \beta\right)\right] \tag{A.21}$$

which corresponds to Eq. (9) in the main text.

References

[1] D. Marpaung, J. Yao, J. Capmany, Integrated microwave photonics, Nat. Photonics 13 (2019) 80–90, http://dx.doi.org/10.1038/s41566-018-0310-5.

[2] S. Yoo, Wavelength conversion technologies for wdm network applications, J. Lightwave Technol. 14 (1996) 955–966, http://dx.doi.org/10.1109/50.511595.

[3] V. Duran, L. Djevarhidjian, H.G. de Chatellus, Bidirectional frequency-shifting loop for dual-comb spectroscopy, Opt. Lett. 44 (2019) 3789–3792, http://dx.doi.org/10.1364/OL.44.003789.

[4] S. Gao, R. Hui, Frequency-modulated continuous-wave lidar using I/Q modulator for simplified heterodyne detection, Opt. Lett. 37 (2012) 2022–2024, http://dx.doi.org/10.1364/OL.37.002022.

[5] C. Quevedo-Galan, A. Perez-Serrano, I.E. Lopez-Delgado, J.M.G. Tijero, I. Esquivias, Dual-comb spectrometer based on gain-switched semiconductor lasers and a low-cost software-defined radio, IEEE Access 9 (2021) 92367–92373, http://dx.doi.org/10.1109/ACCESS.2021.3091872.

[6] L. Shao, N. Sinclair, J. Leatham, Y. Hu, M. Yu, T. Turpin, D. Crowe, M. Lončar, Integrated microwave acousto-optic frequency shifter on thin-film lithium niobate, Opt. Express 28 (2020) 23728–23738, http://dx.doi.org/10.1364/OE.397138.

[7] E.A. Kittlaus, W.M. Jones, P.T. Rakich, N.T. Otterstrom, R.E. Muller, M. Rais-Zadeh, Electrically driven acousto-optics and broadband non-reciprocity in silicon photonics, Nat. Photonics 15 (2021) 43–52, http://dx.doi.org/10.1038/s41566-020-00711-9.

[8] M. Izutsu, S. Shikama, T. Sueta, Integrated optical ssb modulator/frequency shifter, IEEE J. Quantum Electron. 17 (1981) 2225–2227, http://dx.doi.org/10.1109/LPT.2020.3014221.

[9] H. Yamazaki, T. Saida, T. Goh, S. Mino, M. Nagatani, H. Nosaka, K. Murata, Dual-carrier dual-polarization iq modulator using a complementary frequency shifter, IEEE J. Sel. Top. Quantum Electron. 19 (2013) 175–182, http://dx.doi.org/10.1109/JSTQE.2013.2263120.

[10] M. Lauermann, C. Weimann, A. Knopf, W. Heni, R. Palmer, S. Koeber, D.L. Elder, W. Bogaerts, J. Leuthold, L.R. Dalton, C. Rembe, W. Freude, C. Koos, Integrated optical frequency shifter in silicon-organic hybrid (SoH) technology, Opt. Express 24 (2016) 11694–11707, http://dx.doi.org/10.1364/oe.24.011694.

[11] N. Andriolli, F. Fresi, F. Bontempi, A. Malacarne, G. Meloni, J. Klamkin, L. Poti, G. Contestabile, InP monolithically integrated coherent transmitter, Opt. Express 23 (2015) 10741–10746, http://dx.doi.org/10.1364/OE.23.010741.

[12] L.A. Coldren, S.W. Corzine, M.L. Mašanović, Diode Lasers and Photonic Integrated Circuits, John Wiley Sons, Inc., 2012.

[13] J. Zhang, J. Yu, N. Chi, Y. Shao, L. Tao, J. Zhu, Y. Wang, Stable optical frequency-locked multicarriers generation by double recirculating frequency shifter loops for Tb/s communication, J. Lightwave Technol. 30 (2012) 3938–3945, http://dx.doi.org/10.1109/JLT.2012.2206371.

[14] H. Yamazaki, T. Saida, T. Goh, S. Mino, M. Nagatani, H. Nosaka, K. Murata, Dual-carrier dual-polarization IQ modulator using a complementary frequency shifter, 19, 2013, pp. 175–182, http://dx.doi.org/10.1109/JSTQE.2013.2263120.

[15] S. Andreou, K.A. Williams, E.A.J.M. Bente, Steady-state analysis of the effects of residual amplitude modulation of InP-based integrated phase modulators in pound–drever–hall frequency stabilization, IEEE Photonics J. 11 (2019) 1–14, http://dx.doi.org/10.1109/JPHOT.2019.2915163.

[16] J.-F. Vinchant, J. Cavailles, M. Erman, P. Jarry, M. Renaud, InP/GaInAsP guided-wave phase modulators based on carrier-induced effects: theory and experiment, J. Lightwave Technol. 10 (1992) 63–70, http://dx.doi.org/10.1109/50.108738.

[17] S. Kumar, M.J. Deen, Fiber Optic Communications: Fundamentals and Applications, John Wiley Sons, Inc., 2014.

[18] Vpicomponentmaker photonic circuits, 2023, URL https://www.vpiphotonics.com/Tools/PhotonicCircuits.

[19] Nazca design, 2023, URL https://nazca-design.org/.

[20] Smart photonics, 2023, URL https://smartphotonics.nl.

[21] Jeppix (joint european platform for photonic integration of components and circuits), 2023, URL https://www.jeppix.eu.

[22] L.M. Augustin, R. Santos, E. den Haan, S. Kleijn, P.J.A. Thijs, S. Latkowski, et al., InP-based generic foundry platform for photonic integrated circuits, IEEE J. Sel. Top. Quantum Electron. 24 (2018) 1–10, http://dx.doi.org/10.1109/JSTQE.2017.2720967.

[23] M. Smit, X. Leijtens, H. Ambrosius, E. Bente, J. van der Tol, et al., An introduction to InP-based generic integration technology, Semicond. Sci. Technol. 29 (8) (2014) 083001, http://dx.doi.org/10.1088/0268-1242/29/8/083001.

[24] L.V. Keldysh, The effect of a strong electric field on the optical properties of insulating crystals, J. Exptl. Theoret. Phys. (U.S.S.R.) 34 (1958) 1138–1141, http://dx.doi.org/10.1142/9789811279461_0003.